CARBON 57 (2013) 50–58

Available at www.sciencedirect.com

SciVerse ScienceDirect

journal homepage: www.elsevier.com/locate/carbon

Probing the electronic structure of multi-walled carbon nanotubes by transient optical transmittivity

Gianluca Galimberti [a], *Stefano Ponzoni* [a], *Andrea Cartella* [a], *Matthew T. Cole* [b], *Stephan Hofmann* [b], *Cinzia Cepek* [c], *Gabriele Ferrini* [a], *Stefania Pagliara* [a,*]

[a] *Interdisciplinary Laboratory for Advanced Materials Physics (i-LAMP) and Dipartimento di Matematica e Fisica, Università Cattolica del Sacro Cuore, I-25121 Brescia, Italy*

[b] *Department of Engineering, University of Cambridge, 9 JJ Thomson Avenue, Cambridge CB3 0FA, United Kingdom*

[c] *Istituto Officina dei Materiali – CNR, Laboratorio TASC, Area Science Park, Basovizza, I-34149 Trieste, Italy*

ARTICLE INFO

Article history:
Received 14 November 2012
Accepted 13 January 2013
Available online 31 January 2013

ABSTRACT

High-resolution time resolved transmittivity measurements on horizontally aligned free-standing multi-walled carbon nanotubes reveal a different electronic transient behavior from that of graphite. This difference is ascribed to the presence of discrete energy states in the multishell carbon nanotube electronic structure. Probe polarization dependence suggests that the optical transitions involve definite selection rules. The origin of these states is discussed and a rate equation model is proposed to rationalize our findings.

1. Introduction

An understanding of the optical transitions and the underlying electronic structure of carbon nanotubes is of central importance to their characterization and integration within numerous opto-electronic applications.

For single-walled carbon nanotubes (SWCNTs) the density of states, which is dependent on the nanotube chirality and dominated by multiple Van Hove singularities (VHSs), is well defined. The excitonic nature of the optical transitions has been explored in some detail [1–3]. Conversely, multi-walled carbon nanotubes (MWCNTs) represent a much more challenging electronic system and, as yet, no coherent understanding of their properties has been presented.

The presence of multiple, concentrically nested nanotubes, each with differing chirality, greatly complicates the electronic structure of MWCNTs. Theoretical and experimental studies predict similarities between the electronic properties of highly oriented pyrolitic graphite (HOPG) and MWCNTs, however conflicting reports also suggest the presence of discrete states which make MWCNTs more similar to SWCNTs [4,5].

Multiple shells enhance the electrical conductivity due to several distinct transport pathways [6–9]. Moreover a larger absorption cross-section results with high spectral absorbance over the entire visible spectrum [10–12]. MWCNTs are consequently extremely promising for photovoltaic applications, in particular when used in conjunction with various electron donor groups [8,13]. Higher incident-photon-to-current efficiencies (IPCE) have been observed for MWCNTs compared to SWCNTs [8]. Key to such future applications, however, is a more detailed understanding of their underlying electronic and optical properties.

Here, we employ time-resolved optical spectroscopy to critically compare the transient optical response of MWCNTs and HOPG.

Highly aligned suspended MWCNT films have been employed to negate detrimental substrate contributions. Horizontal alignment ensures that the probed electronic structure is unaffected by variable sample features, such as nanotube curvature [14].

By performing monochromatic transient transmittivity experiments, in the near-infra-red (790 nm), we demonstrate

* *Corresponding author:* Fax: +39 (030)2406 742.
E-mail address: pagliara@dmf.unicatt.it (S. Pagliara).
0008-6223/$ - see front matter
http://dx.doi.org/10.1016/j.carbon.2013.01.030

the presence of discrete energy states in the MWCNT electronic structure. In this framework, the transient response is characterized by photo-bleaching (PB) and photo-absorption (PA) channels, as well as non-linear effects that we control by tuning the probe polarization.

The dependence on the probe polarization unambiguously shows that these states have a well-defined symmetry and that the optical transitions between these states respect precise selection rules. Two different interpretations are proposed and discussed to account for these states: the first concerns the presence of clusters in the nanotube walls. The second one hypothesizes a MWCNT electronic structure similar to that of SWCNTs and, although many questions remain still open, it appears more consistent with the experimental results here reported.

2. Experimental

2.1. Sample preparation

The carbon nanotubes (CNTs) investigated were aligned, free-standing MWCNTs, synthesized by thermal chemical vapor deposition in a commercially available, cold-wall reactor (Aixtron Ltd.). Vertically aligned nanotube forests were grown on thermally oxidized Si substrates (200 nm SiO_2) coated with 10 nm Al_2O_x (magnetron sputtered) and 1 nm Fe (thermally evaporated). Bilayer catalysts were heated to 700 °C (5 °C/s) under 8 sccm C_2H_2 diluted in 192 sccm H_2 (25 mbar). Aligned, free-standing MWCNT thin films were fabricated by solid-state pulling at a rate of $\sim 10^{-2}$ m/s, as illustrated in the insert of Fig. 1a, employing a similar technique as reported elsewhere [15]. MWCNT bundles were pulled mechanically from a pristine source nanotube forest, several hundred micrometers in length, allowing us to obtain continuous yarns/thin films of high-purity MWCNTs. Fig. 1a shows an optical micrograph of a vertically aligned MWCNT forest during membrane solid-state pulling. To ensure the probed characteristics are associated implicitly with the MWCNTs, no post-growth chemical processing was performed (Fig. 1a). In the inset, a cross-section schematic of a catalyst wafer is shown. Fig. 1b shows a scanning electron micrograph (SEM) of the aligned, free-standing MWCNT film. High-resolution transmission electron microscopy (HR-TEM) clearly shows multiple graphitized side-walls (Fig. 1b, inset) with negligible *amorphous carbon* deposits and minimal bamboo-like sectioning. The as-grown MWCNTs were approximately 500 μm in length, 25 ± 13 SD (Standard Deviation) nm in diameter and consisted of typically 2–5 graphitic walls. In Fig. 1c the histograms, showing the outer diameter and number of graphitic walls (Inset) are reported. Highlighted areas denote the mean ± 1 SD. Fig. 1d shows a typical Raman spectra (Renishaw InVia, 633 nm excitation, 3 mW) of the film at multiple positions, evidencing the high sample uniformity. X-ray photoelectron spectroscopy (XPS), Raman spectroscopy and HR-TEM confirm the high graphitic quality of the MWCNTs (see Supporting information).

Ultra violet photoelectron spectroscopy (UPS) was acquired in a ultra-high vacuum chamber using a conventional He discharge lamp ($h\nu$ = 21.2 eV) and a hemispherical electron energy analyzer. The electron energy distribution curves were measured at room temperature in normal emission geometry, with an overall instrumental energy resolution of ~0.1 eV. The binding energy scales are referred to the Fermi level of a gold polycrystal foil.

Free-standing, well-aligned horizontal MWCNTs permit strict control over the relative angles between the MWCNTs and the incident polarization, whilst simultaneously avoiding detrimental substrate optical interference effects. Herein "perpendicular-polarized" is defined as the light polarization perpendicular to the MWCNT long-axis and "parallel-polarized" as the polarization parallel to the MWCNT long-axis.

2.2. Laser system

Samples were optically excited using a Ti: Sapphire cavity-dumped, mode-locked laser oscillator. Output pulses were centered at 790 nm (1.55 eV) with a full-width half-maximum of 120 fs. The output energy was 50 nJ (per pulse) with a variable repetition rate from 54.3 MHz to a single shot. Mean heating effects were obviated using tunable repetition rates. The pump fluence ranged from 0.1 to 0.8 mJ/cm^2. Low fluence measurements were obtained at 540 kHz to maximize the signal-to-noise ratio. A lock-in acquisition technique was employed to provide high resolution in the transient transmittivity signal ($\Delta T/T$).

3. Results and discussion

It is known that in MWCNTs the presence of different nanotubes, each with different diameter and chirality, smooths the VHSs, resulting in an electronic structure similar to that of the HOPG [3,5]. This is in agreement with static absorption measurements, performed using an ultraviolet–visible-near infrared spectrometer (Fig. 1e), where no particular absorption peaks, characteristic of the VHSs, are evident, in agreement with a HOPG-like electronic structure. The absorption data confirms the alignment of our MWCNTs. When the incident polarization is parallel to the MWCNT long-axis (denoted 'par'), the absorption is larger than in the perpendicular case (denoted 'perp').

In order to compare the transient electronic behavior of MWCNTs and HOPG, we have performed monochromatic transient transmittivity ($\Delta T/T$) measurements, shown in Fig. 2, where the pump and the probe photon energy is 1.55 eV and the pump fluence is fixed at 0.25 mJ/cm^2 (~10^{15} - photons/cm^2). Fig. 2a shows the transient transmittivity collected by rotating the probe polarization, from parallel to perpendicular to the MWCNT long-axis, with the pump polarization fixed parallel to the MWCNT long-axis. To clearly evidence the probe polarization dependence of the transient signal, in Fig. 2a $\Delta T/T$ data have been normalized to the first $\Delta T/T$ maximum (at zero delay time). The shape of the transient response is unmodified by the normalization procedure.

Two dynamics dominate the MWCNT response. The first, observed at short delay times (<150 fs), is positive and consistent with a PB, previously observed in HOPG and SWCNTs [1,2,14,16,17]. Charge carriers are promoted by the pump from the ground state to an excited state and the absorption of the

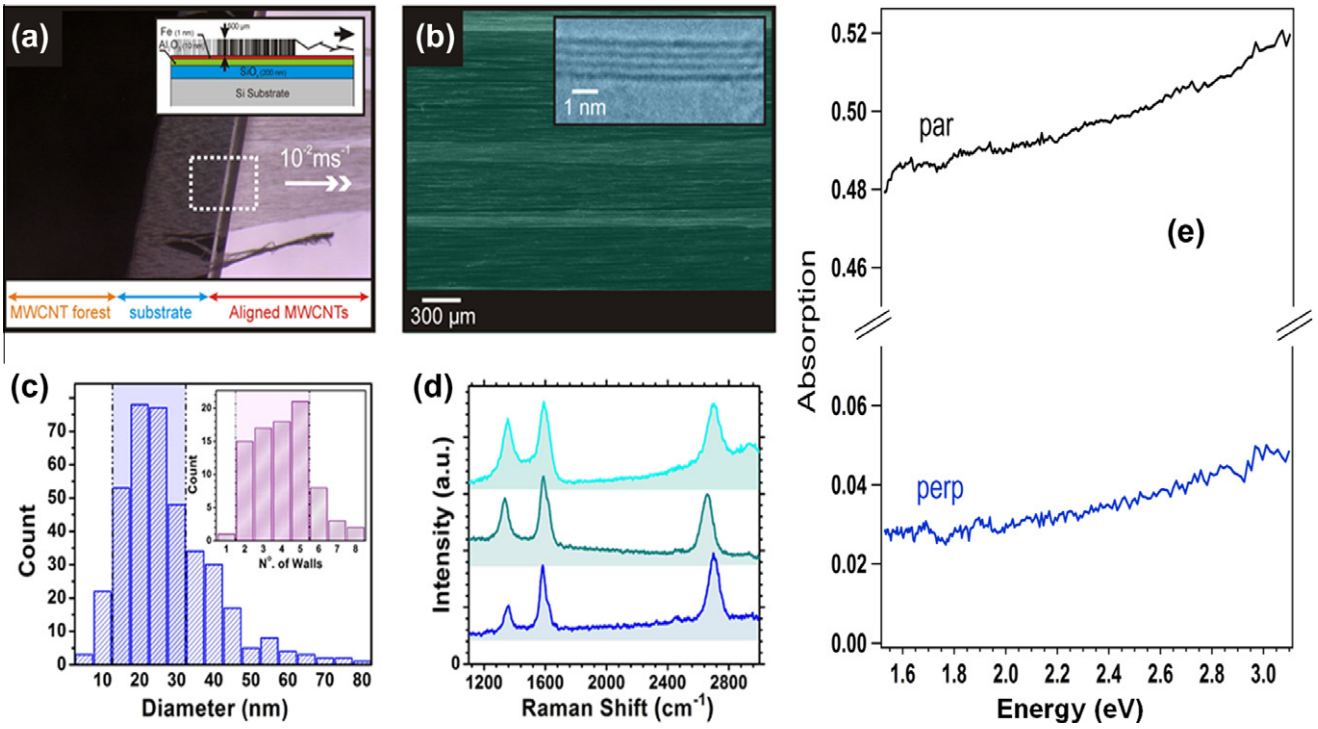

Fig. 1 – (a) Optical micrograph of a vertically aligned MWCNT forest during membrane solid-state pulling. Inset: Cross-section schematic of a catalyst wafer. (b) SEM micrograph of an aligned MWCNT membrane (Scale bar: 300 μm). Inset: HR-TEM micrograph showing the graphitic side-walls of the thermal chemical vapor deposited MWCNTs (scale bar: 1 nm). (c) Histograms showing the outer diameter and number of graphitic walls (Inset). Highlighted areas denote the mean ± 1 Standard Deviation (d) Raman spectra (633 nm, 3 mW) of an as-grown MWCNT forest (top) and an extruded membrane (middle, bottom). Negligible variation was noted in the acquired spectra across samples. (e) Static absorption as a function of energy.

probe, at the same photon energy, decreases due to final state filling, with a corresponding enhancement of the probe transient transmission. The intensity of this PB feature, for a constant pump fluence, is affected by coherence effects that strongly enhance the signal when the pump and probe polarizations are parallel to one another [18,19].

The second dynamic (>150 fs) occurs over a temporal range independent of any coherence effects and, unlike the first, depends strongly on the probe polarization. In particular, the sign of this second response is negative when the probe polarization is parallel to the MWCNT long-axis and positive when perpendicular to it. By rotating the probe polarization relative to the MWCNT long-axis, from 0° (parallel-polarized) to 90° (perpendicular-polarized), the second dynamic changes sign – from negative to positive.

The change of sign depends exclusively on the probe polarization. To exclude a pump polarization contribution, in Fig. 2b while keeping a fixed parallel-polarized probe, the pump polarization is rotated (at 10° increments), obtaining a variation of the second dynamic intensity. The magnitude of this second dynamic is consistently negative for all pump polarizations. Similarly, fixing the probe perpendicular-polarization (Fig. 2c), the rotation of the pump polarization changes only the intensity of the second dynamic, maintaining the positive sign.

The optical response with parallel-polarized probe (Fig. 3a) has been interpolated by two exponential functions, convoluted with a Gaussian representing the pulse temporal width. While the first dynamic, affected by the presence of the coherent artifact, is very fast (40 ± 15 fs), the second is an order of magnitude slower (400 ± 100 fs). The analysis of the optical response with perpendicular-polarized probe (Fig. 3b), performed with the same fitting procedure, gives a similarly fast first dynamics (40 ± 15 fs), while the second is 1.0 ± 0.1 ps.

The surprising dependence of the second dynamic on the probe polarization allows us to grasp, for the first time, the difference between the transient behavior of MWCNTs and HOPG.

While the positive PB response, in fact, appears consistent with the HOPG-like behavior, the negative response (probe polarization parallel to MWCNT long-axis, Fig. 3a) excludes a HOPG-like relaxation channel. With a parallel-polarized pulse only the component of the dielectric constant parallel to the MWCNT long-axis is probed, corresponding to the component of the HOPG dielectric constant perpendicular to the graphite c-axis [11,20,21]. Under equivalent experimental conditions, the HOPG transient response reveals only PB channels. Two exponential decays, ascribed to electron–electron and electron–phonon relaxation, in agreement with the two temperatures model [22–24], are, in fact, measured in the transient reflectivity signal (Fig. 3c (top)).

Under different experimental conditions a negative dynamic has also been reported in HOPG and ascribed to

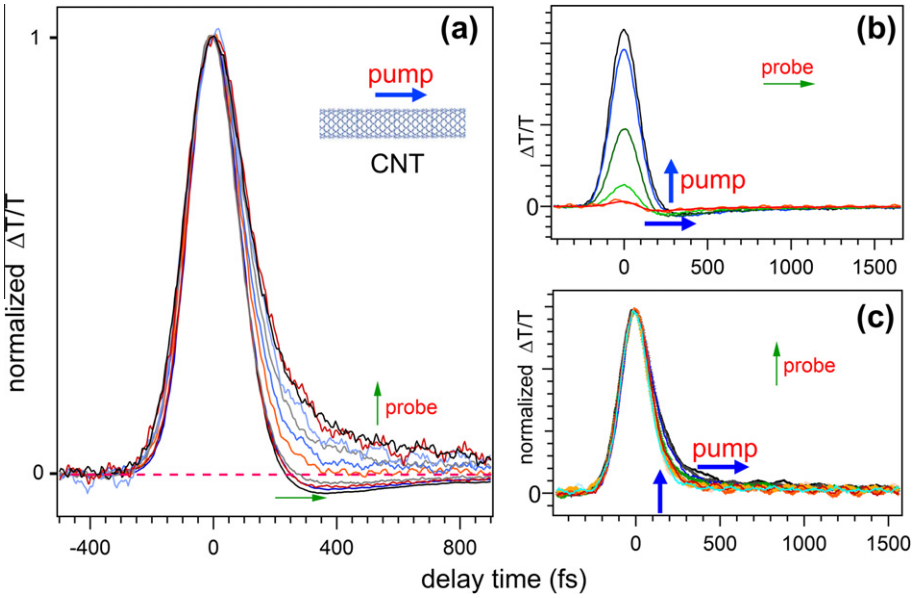

Fig. 2 – (a) Monochromatic normalized transient transmittivity ($\Delta T/T$), at 1.55 eV, collected with a pump polarization parallel to the MWCNTs long-axis and the probe polarization varying from parallel to perpendicular. (Incident fluence = 0.25 mJ/cm^2). The sign of the second dynamic depends only on the probe polarization and varies continuously from negative (probe polarization parallel to MWCNT long-axis) to positive (probe polarization perpendicular to MWCNT long-axis). Spectra are normalized to the maximum response of the positive signal (1.3×10^{-3}), excluding coherence-artifacts. Non-normalized and normalized dependence of $\Delta T/T$ with probe polarization parallel (b) and perpendicular (c) to the MWCNT long-axis, respectively. The pump polarization rotation does not affect the sign of the second dynamic. For pump fluences $\leqslant$ 0.25 mJ/cm^2, the intensity of the second dynamic tracks the laser pump absorption that depends on the angle between the laser polarization and the MWCNT long-axis[10]. The oscillations in (b) and (c) have an intensity below the instrument sensitivity ($\Delta T/T \approx 10^{-6}$).

intra-band transitions (Drude model). For observing these intra-band transitions in HOPG and graphene layers, the probe photon energy is usually in the terahertz range [25–29]. In the high pump fluence regime, oscillations have been observed in the HOPG transient signal and ascribed to structural deformation of the inter-plane separation due to strongly-coupled-optical-phonons [30,31]. However, such structural deformation can be excluded in MWCNTs since structural oscillations of the graphitic walls, observed in SWCNTs, depend strongly on the pump polarization and not on the probe polarization, as revealed in Fig. 2. Moreover, the period of these oscillations is fast [16,32,33].

This surprising and significant difference between the transient behavior of MWCNTs and HOPG is also confirmed by the pump–probe delay dependence of the MWCNT inverse transient transmittivity ($(\Delta T/T)^{-1}$) in the range of the positive second dynamics (probe polarization perpendicular to the MWCNT long-axis, Fig. 3b). In Fig. 3c, the pump–probe delay dependence of the absolute value of the HOPG inverse transient reflectivity ($(\Delta R/R)^{-1}$, top) is shown together with the MWCNT $(\Delta T/T)^{-1}$ (bottom).

The linear dependence, shown in Fig. 3c (bottom), for MWCNTs suggests the non-linear character of the second dynamic. For example, the existence of a quadratic dependence implies the following relation [34–36]:

$$\frac{dN}{dt} \propto N^2 \tag{1}$$

and consequently:

$$\left(\frac{\Delta T}{T}\right)^{-1} \propto \Delta t \tag{2}$$

where N is the photo-excited carriers density population and Δt is the delay time between pump and probe pulse. The linear behavior (Fig. 3c (bottom)) of the MWCNT transient response, for delay times >500 fs, reveals the non-linear character of the second dynamic, when the probe is perpendicular-polarized.

On the contrary, the non-linear HOPG dependence of $|(\Delta R/R)^{-1}|$ on the pump–probe delay (Fig. 3c (top)), confirms that the two dynamics in the HOPG transient signal are consistent with the two-temperature model. We assume here, as suggested by Fig. 3c, that the second dynamic of MWCNTs was a second order process.

This unexpected difference in the transient behavior of MWCNTs and HOPG can be explained by considering localized electronic states.

The presence of discrete levels in the MWCNT electronic structure permits also to justify the negative dynamic. Charge carriers, photo-excited by the pump in a previously well-defined unoccupied state, are promoted from this energy state to a higher one by the probe, resulting in a decrease of the transient transmittivity of the probe (negative signal). This process is known in literature as PA effect.

At the same time, the second positive dynamic can be ascribed to a re-filling of an unoccupied state by second order processes.

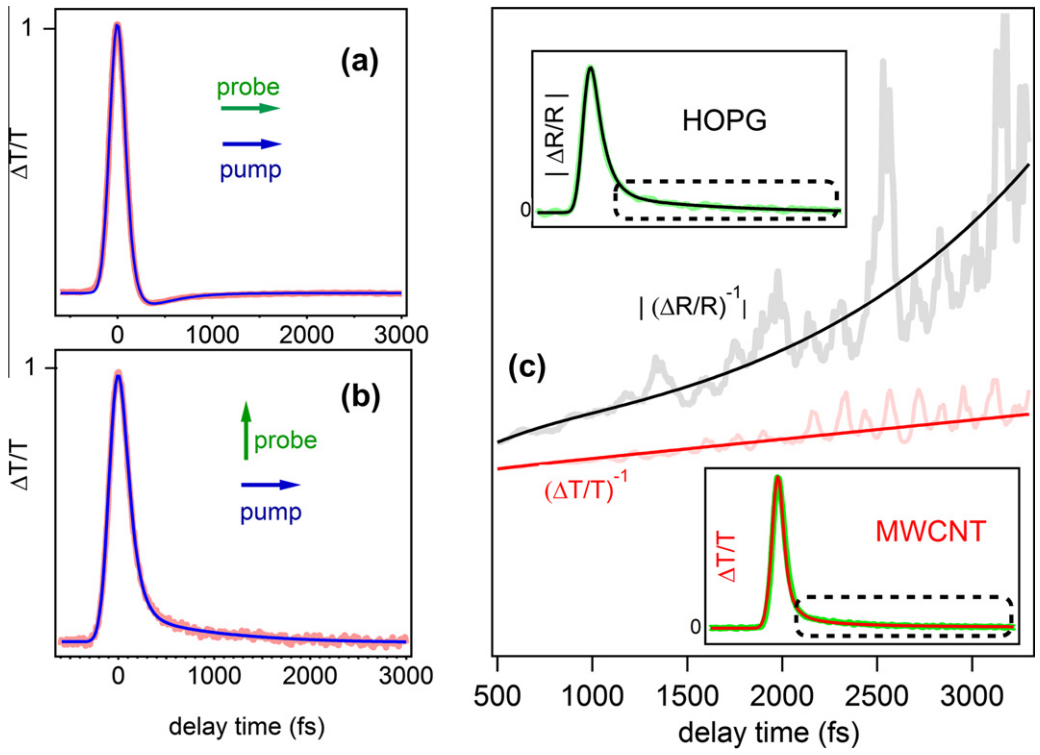

Fig. 3 – (a) ΔT/T for pump and probe polarizations parallel to the MWCNT long-axis. Fit (blue) of the experimental data (red), as modeled by Eq. (3). (b) ΔT/T for pump polarization parallel and probe polarization perpendicular to the MWCNT long-axis. Fit (blue) of the experimental data (red) as modeled by Eq. (3). (c) Top: $|(\Delta R/R)^{-1}|$ of the HOPG (inverse of the fit extracted from the inset) as a function of the delay time (0.5–2.5 ps). Bottom: $(\Delta T/T)^{-1}$ of MWCNTs (inverse of the fit extracted from the inset) as a function of the delay time (0.5–2.5 ps). Note the linearity. Spectra collected with pump polarization parallel and probe polarization perpendicular to the MWCNTs long-axis. (For interpretation of the references to color in this figure legend, the reader is referred to the web version of this article.)

To account for the transient optical behavior, we propose a model of the involved optical transitions based on three discrete electronic states, as illustrated in Fig. 4. The pump excites ground state carriers (E_0), to a higher state (E_2), that within a few tens of femtoseconds decays to lower energy state (E_1). The probe pulse at the same pump photon energy (1.55 eV), when parallel-polarized with respect to the tube axis, reveals firstly a PB due to the filling of E_2, then, for longer delay times, promotes electrons from E_1 to a higher state (E_3). In the transient transmission spectra, this last process corresponds to an enhancement of the probe absorption (PA) thereby producing the negative ΔT/T response (Fig. 4a and b).

When the probe polarization is perpendicular to the MWCNT long-axis, the probe reveals two PB channels. Charge carries are promoted by the pump from the ground state to E_2 (first PB) that relaxes within 100 fs from E_2 to E_1. The probe then, for longer delay times, reveals a second PB of E_0–E_2 due to a re-population of E_2 by second order processes (Fig. 4c and d).

The strong dependence of the second dynamic on the probe polarization unambiguously suggests that the relaxation processes involve localized energy states with a well-defined symmetry [37,38] and that the optical transitions between these states observe precise selection rules.

The PA channel is quenched when the probe is perpendicular-polarized. On the contrary, in this configuration, due to the high pump fluence (10^{14}–10^{15} photons/cm^2) and to the long E_1 decay time (few picoseconds [37]), second order processes are favored thereby repopulating E_2. These second order processes increase the transmittivity of the probe resulting in a second PB channel.

The choice of three localized energy states (E_1, E_2, E_3) is in accord with the analysis of the decay times. The PA implies a transition of the photo-excited carriers to a higher state. However, the decay time of the first state, filled by the pump, is really very fast (<100 fs) and is inconsistent with the PA relaxation time (hundreds of fs). Therefore a third energy state, with a longer decay time, must be considered as a starting level for PA.

To better rationalize our findings, we propose a rate equation model to interpret the relaxation processes depicted in Fig. 4. The temporal evolution of the photo-excited carriers on the E_2 state (N_2) and on the E_1 (N_1) is then determined by:

$$\begin{aligned}\frac{\partial N_2}{\partial t} &= A\cdot G(t) - B\cdot N_2 + \tfrac{C}{2}\cdot N_1^2 \\ \frac{\partial N_1}{\partial t} &= B\cdot N_2 - D\cdot N_1 - C\cdot N_1^2\end{aligned} \qquad (3)$$

where E_2 is populated by the Gaussian pump $G(t) = (\sigma\sqrt{2\pi})^{-1} e^{-\frac{t^2}{2\sigma^2}}$ and depopulated by the -BN_2 term with B^{-1} corresponding to the N_2 decay time ($E_2 \rightarrow E_1$). The $CN_1^2/2$ term represents the second order process able to populate the E_2 state starting from E_1. In agreement with the first rate equation, E_1 is populated by the electron relaxation from E_2

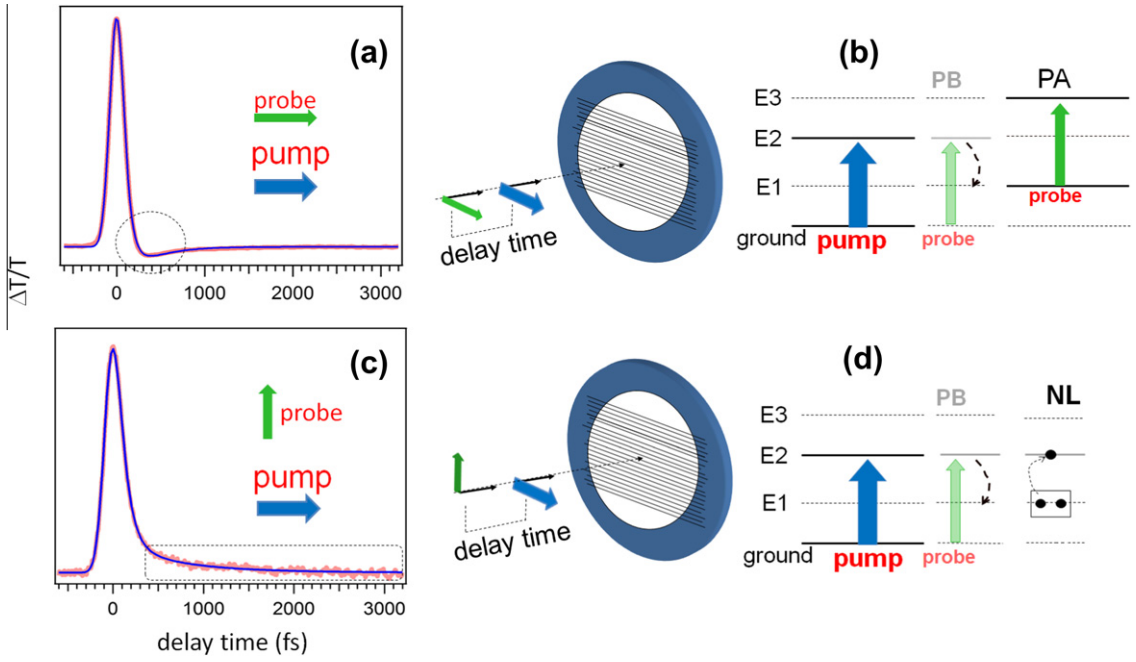

Fig. 4 – (a) ΔT/T for pump and probe polarizations parallel to the MWCNT long-axis. Fit (blue) of the experimental data (red), as modeled by Eq. (3). (b) Schematic of the relaxation channels (PB, and PA) as rationalized in the proposed model. (c) As in (a), ΔT/T signal (red) and fitting (blue) for pump polarization parallel and probe polarization perpendicular to the MWCNT long-axis. (d) Schematic of the relaxation channels (PB and non linear process) (For interpretation of the references to color in this figure legend, the reader is referred to the web version of this article.).

(BN_2) and depopulated by the relaxation on the ground state ($-DN_1$) and the second order processes ($-CN_1^2$). The $\Delta T/T$ signal has been interpolated, in a non-perturbative approach, *via* the expression:

$$\frac{\Delta T}{T} \propto N_2 - \alpha_{PA} \cdot N_1 \qquad (4)$$

where α_{PA} is linearly proportional to the magnitude of the PA.

The transient responses, given in Fig. 4a and c, for the parallel- and perpendicular-polarized probe, are well interpolated by the proposed model (blue line fit, red line data). The C parameter, that represents the second order process weight, was fixed as the pump fluence did not change throughout the measurements. The mean fitted B^{-1} value, for the different spectra, is 60 ± 20 fs. For the perpendicular-polarized probe spectra, the D^{-1} decay time is a few picoseconds, corresponding to the long decay of the lower E_1 state. In the case of parallel-polarized probe spectra (with negative PA dynamics), D^{-1} is a few hundred of femtoseconds.

In Fig. 5, the fitted α_{PA} value, representing the PA weight, is shown as a function of the angle between the probe polarization and MWCNT long-axis. $\alpha_{PA} = 0$ when the angle is 90°, as the selection rule prevents PA. Increasing the component of the probe polarization along the MWCNT long-axis, angle <45°, the PA, again in agreement with the dipole selection rules, begins to increase, reaching the maximum value when the polarization direction is along the MWCNT long-axis. To further elucidate the PA promotion mechanism, rather than the non-linear mechanism, in the second dynamic, in Fig. 6a the dependence of the PA channel on the pump fluence is shown by fixing the probe polarization parallel to the

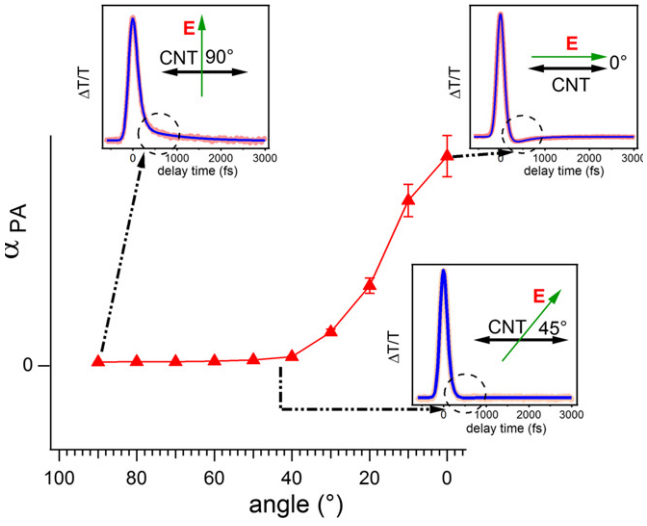

Fig. 5 – PA coefficient, α_{PA}, Eqs. (3) and (4) as a function of the angle between the probe polarization and the MWCNT long-axis. When the probe polarization is perpendicular, PA is quenched (top left inset). PA becomes non-zero around 45° (bottom right inset) and reaches a maximum when the probe polarization is parallel (top right inset).

MWCNT long-axis. By increasing the fluence, saturation is clearly noted, as highlighted in more detail in Fig. 6b where the PA (maximum) *versus* the pump fluence is plotted. This saturation effect can be explained by considering that, as the non-linear channel quadratically increases with fluence,

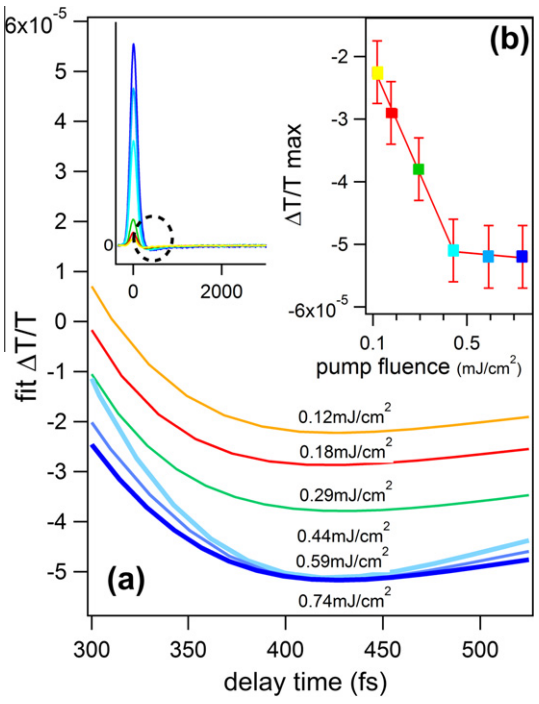

Fig. 6 – (a) Interpolated ΔT/T (inset) dependence on increasing pump fluence. The saturation effect of PA channel (second negative dynamic) is shown in (b) by plotting the maximum value of the ΔT/T relative to the PA effect *versus* the pump fluence.

the resulting non-linear optical response increases much more rapidly than the linear PA of the probe. Thus, the latter saturates. PA is then quenched by rotating the probe polarization (from parallel to perpendicular) or by increasing the pump fluence. In this second case, the enhanced photo-excited carriers density, corresponding to an increased second order process, repopulates E_2 whose relaxation is described by the second positive dynamic (Fig. 4c).

In light of the obtained results, we emphasize that the surprising presence of localized states in MWCNT electronic structure can be also confirmed by static photoemission and static absorption spectroscopy.

The analysis of the photoemission valence band (Fig. 7a), collected with He I radiation source (21.2 eV) clearly shows two broad features (~1.0 and 3.0 eV). While the second is ascribed to the π band [39], the large feature centered at about 1.0 eV suggests the presence of occupied states under 3.0 eV. Furthermore, the absence of electronic states at the Fermi energy (inset of Fig. 7a) indicates a semi-metallic character. This result is in agreement with transport studies, undertaken in a vacuum pumped cryostat (297–16 K), that show a nominal band gap of approximately 40 meV, consistent with that of other semi-metallic graphitic materials.[1]

Moreover, from the optical spectra (shown in Fig. 1e), we are able to obtain further insight about the presence of electronic structures in the occupied and unoccupied bands. The polarisability, ρ, of the system, is defined as [10,40]:

$$\rho = \frac{\Lambda_{//} - \Lambda_{\perp}}{\Lambda_{//} + \Lambda_{\perp}} \quad (5)$$

where $\Lambda_{//}$ is the absorbance for incident beam polarization parallel and $\Lambda_{\perp}$ perpendicular to the MWCNT long-axis, and $I/I_0 = e^{-\Lambda}$, where $\Lambda = \Lambda_{\perp}$ or $\Lambda_{//}$, I is the intensity of the transmitted beam and I_0 is the incident intensity. As in the case of SWCNTs [40], ρ (Fig. 7b) linearly decreases with photon energy (1.55–3 eV), suggesting the existence of optical transitions with a definite symmetry below 3 eV.

The crucial point remains, now, to understand the origin of discrete energy levels in the electronic structure of MWCNTs. Two possible interpretations can be offered.

The first is connected with the presence of amorphous carbon. sp^3 and sp^2 clusters smaller than 5 nm may very well open a gap thereby instigating the formation of originate discrete levels [41]. Indeed, the existence of electronic states associated with structural defects could represent an interesting opportunity for improving the polarization-controlled absorption in such samples. However, XPS and Raman spectroscopy (see Supporting information) seems to exclude this possibility. Moreover, there is controversy related to this interpretation. Firstly, the results reported in Fig. 2 have been obtained at different positions on different samples grown under equivalent conditions. Furthermore, it is not clear as to how such clusters of amorphous material could give rise to electronic states with well-defined symmetry.

The second interpretation is derived by considering that discrete states are present in the valence band and that the optical transitions, revealed in the transient transmittivity, involve discrete electronic states with a well-defined symmetry. In particular, it is somewhat surprising the analogy between the selection rules of the optical transitions involved in the transient response of MWCNTs and those known for the VHSs in SWCNTs. In this sense this second interpretation assumes that the electronic structure of MWCNTs is characterized, as in the case of SWCNTs, by the presence of excitonic states at the VHSs. Assuming, in fact, that the processes reported in Fig. 4 can be ascribed to excitonic transitions, the polarization dependence of the PA channel (Fig. 4a and b) is consistent with the selection rules that control the SWCNT optical transition. For a parallel-polarized probe, the PA corresponding to $\Delta m = 0$, where m is the quantum number identifying the VHSs sub-bands [37], is allowed. On the contrary, when the probe is perpendicularly-polarized the PA is quenched and a second order decay process dominates (Fig. 4c and d). This alternative channel might appear similar to exciton–exciton annihilation (EEA), well studied on spatially confined systems such as nanocrystals [42] and more recently reported in SWCNTs [34–36,43,44]. EEA refills E_{22} and increases the transmittivity of the probe resulting in a second PB channel. The non-linear character of EEA could be compatible with the linearity of the $(\Delta T/T)^{-1}$, shown in Fig. 3. The rate Eq. (3) are very similar to the rate equations model employed in literature [34–36,44] to describe the excitonic behavior of SWCNTs in a high pump fluence regime. This SWCNT-like behavior could be also confirmed by considering the relaxation times. The first dynamic of the MWCNTs has a relaxation

[1] Unpublished data.

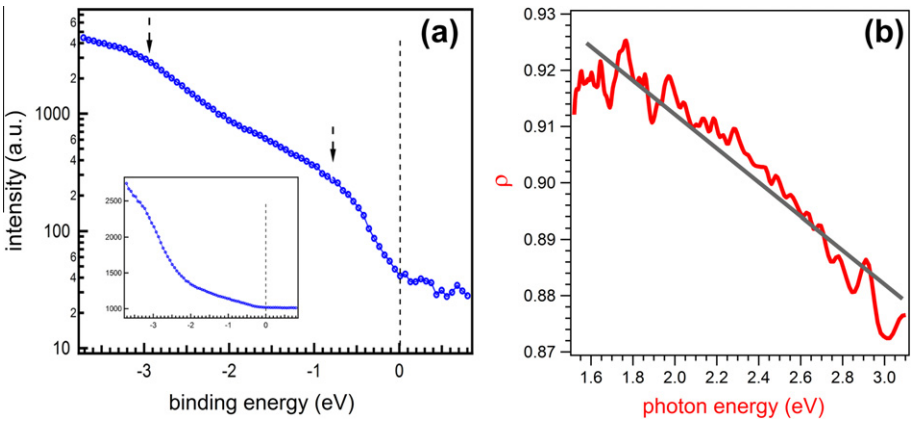

Fig. 7 – (a) UPS measurements of the valence band showing broad features at about 1.0 and 3 eV (log. scale). Inset: Detailed valence band, suggesting a semi-metallic character consistent with temperature dependent electron transport studies. (b) Static polarizability ρ as a function of photon energy.

time (60 ± 20 fs) consistent with the E_{22}-to-E_{11} transition in SWCNTs (~40 fs) [1,2]. Similarly the PA has a recovery time of the order of hundreds of femtoseconds [2], comparable with the E_{11}-to-E_{33} absorption channel in SWCNTs.

This second interpretation, concerning the presence of excitonic states at the VHS, despite requires further confirmations, provides a more consistent depiction of the transient electronic behavior of MWCNTs. Moreover, it corroborates recent measurements reported in literature where it was shown that the VHSs play an important role in the electronic behavior of MWCNTs [4,8,45,46].

4. Conclusions

Using high-resolution time resolved transmittivity measurements on horizontally aligned free-standing MWCNTs, we have shown that the electronic structure of these systems is different from that of HOPG. The optical response of MWCNTs is seen to be characterized by photo-bleaching and photo-absorption processes as well as second order effects. We are able to reveal these transient channels tuning the probe polarization. The obtained results suggest the existence of discrete levels with a well-defined symmetry in the electronic structure of MWCNTs. Two different interpretations have been discussed. The origin of these states appears more consistent with a SWCNT-like interpretation. It is hoped that this study will provide a deeper understanding of the so-far largely misunderstood and complex electronic structure of MWCNTs, showing, for the first time, the presence of discrete levels in these complex systems. An improved understanding of these issues, and the possibility of polarization-selective control over the optical response of MWCNTs represent important aspects in the outlook of carbon nanotube research.

Acknowledgments

M-T-C wishes to thank St. Edmunds College Cambridge and the Isaac Newton Trust for generous financial support.

S-P and G-F acknowledge partial support from D.2.2 grants of the UCSC.

The authors' thank the Cavendish Laboratory, Cambridge University, for the kind use of the SEM and Raman facilities.

Appendix A. Supplementary data

Supplementary data associated with this article can be found, in the online version, at http://dx.doi.org/10.1016/j.carbon.2013.01.030.

REFERENCES

[1] Korovyanko OJ, Sheng C-X, Vardeny ZV, Dalton AB, Baughman RH. Ultrafast spectroscopy of excitons in single-walled carbon nanotubes. Phys Rev Lett 2004;92(1):017403–17406.
[2] Manzoni C, Gambetta A, Menna E, Meneghetti M, Lanzani G, Cerullo G. Intersubband exciton relaxation dynamics in single-walled carbon nanotubes. Phys Rev Lett 2005;94(20):207401–4.
[3] Lin MF. Optical spectra of single-wall carbon nanotube bundles. Phys Rev B 2000;62(19):13153–9.
[4] Castrucci P, Scilletta C, Del Gobbo S, Scarselli M, Camilli L, Simeoni M, et al. Light harvesting with multiwall carbon nanotube/silicon heterojunctions. Nanotechnology 2011;22(11):115701–9.
[5] Lin MF, Shyu FL, Chen RB. Optical properties of well-aligned multiwalled carbon nanotube bundles. Phys Rev B 2000;61(20):14114–8.
[6] Agrawal S, Raghuveer MS, Ramprasad R, Ramanath G. Multishell carrier transport in multiwalled carbon nanotubes. IEEE Trans Nanotechnol 2007;6(6):722–6.
[7] Agrawal S, Raghuveer MS, Li H, Ramanath G. Defect-induced electrical conductivity increase in individual multiwalled carbon nanotubes. Appl Phys Lett 2007;90(19):193104–6.
[8] Scarselli M, Scilletta C, Tombolini F, Castrucci P, Diociaiuti M, Casciardi S, et al. Multiwall carbon nanotubes decorated with copper nanoparticles: effect on the photocurrent response. J Phys Chem C 2009;113(14):5860–4.
[9] Ngo Q, Petranovic D, Krishnan S, Cassell AM, Ye Q, Li J, et al. Electron transport through metal-multiwall carbon nanotube interfaces. IEEE Trans Nanotechnol 2004;3(2):311–7.
[10] Ni C, Bandaru PR. Enhanced optical absorption cross-section characteristics of multi-wall carbon nanotubes. Carbon 2009;47:2898–903.

[11] Bao H, Ruan X, Fisher TS. Optical properties of ordered vertical arrays of multi-walled carbon nanotubes from FDTD simulations. Opt Express 2010;18(6):6347–59.
[12] Lidorikis E, Ferrari AC. Photonics with multiwall carbon nanotube arrays. ACS Nano 2009;3(5):1238–48.
[13] Kamat PV. Meeting the clean energy demand: nanostructure architectures for solar energy conversion. J Phys Chem C 2007;111(7):2834–60.
[14] Galimberti G, Pagliara S, Ponzoni S, Dal Conte S, Cilento F, Ferrini G, et al. The photoinduced charge transfer mechanism in aligned and unaligned carbon nanotubes. Carbon 2011;49:5246–52.
[15] Jiang K, Li Q, Fan S. Spinning continuous carbon nanotube yarns. Nature 2002;419:801.
[16] Kato K, Ishioka K, Kitajima M, Tang J, Saito R, Petek H. Coherent phonon anisotropy in aligned single-walled carbon nanotubes. Nano Lett 2008;8(10):3102–8.
[17] Hasimoto H, Murakami Y, Maruyama S, Kono J. Anisotropic decay dynamics of photoexcited aligned carbon nanotube bundles. Phys Rev B 2007;75(24):245408–12.
[18] Brito-Cruz CH, Gordon JP, Becker PC, Fork RL, Shank CV. Dynamics of spectral hole burning. IEEE J Quantum Electron 1988;24(2):261–9.
[19] Luer L, Crochet J, Hertel T, Cerullo G, Lanzani G. Ultrafast excitation energy transfer in small semiconducting carbon nanotube aggregates. ACS Nano 2010;4(7):4265–73.
[20] Garcia-Vidal FJ, Pitarke JM, Pendry JB. Effective medium theory of the optical properties of aligned carbon nanotubes. Phys Rev Lett 1997;78(22):4289–92.
[21] Lu W, Dong J, Li Z-Y. Optical properties of aligned carbon nanotube systems studied by the effective-medium approximation method. Phys Rev B 2000;63(3):033401–33404.
[22] Pagliara S, Galimberti G, Mor S, Montagnese M, Ferrini G, Grandi MS, et al. Photoinduced π^* band gap renormalization in graphite. J Am Chem Soc 2011;133:6318–22.
[23] Seibert K, Cho GC, Kutt W, Kurz H, Reitze DH, Dadap JI, et al. Femtosecond carrier dynamics in graphite. Phys Rev B 1990;42(5):2842–51.
[24] Anisimov SI, Kapeliovich BL, Perel'man TL. Electron emission from metal surfaces exposed to ultrashort laser pulses. Sov Phys JETP 1974;39:375–7.
[25] Parrott EPJ, Zeitler JA, McGregor J, Oei S-P, Unala HE, Milne WI, et al. The use of terahertz spectroscopy as a sensitive probe in discriminating the electronic properties of structurally similar multi-walled carbon nanotubes. Adv Mater 2009;21:3953–7.
[26] George PA, Strait J, Dawlaty J, Shivaraman S, Chandrashekhar M, Rana F, et al. Ultrafast optical-pump terahertz-probe spectroscopy of the carrier relaxation and recombination dynamics in epitaxial graphene. Nano Lett 2008;8(12):4248–51.
[27] Kampfrath T, von Volkmann K, Aguirre CM, Desjardins P, Martel R, Krenz M, et al. Mechanism of the far-infrared absorption of carbon-nanotube films. Phys Rev Lett 2008;101(26):267403–6.
[28] Dawlaty JM, Shivaraman Sh, Chandrashekhar MVS, Rana F, Spencer MG. Measurements of ultrafast carrier dynamics in epitaxial graphene. Appl Phys Lett 2008;92(4):042116–42119.
[29] Newson RW, Dean J, Schmidt B, van Driel HM. Ultrafast carrier kinetics in exfoliated graphene and thin graphite films. Opt Express 2009;17(4):2326–33.
[30] Carbone F, Baum P, Rudolf P, Zewail AH. Structural preablation dynamics of graphite observed by ultrafast electron crystallography. Phys Rev Lett 2008;100(3):035501–35504.
[31] Carbone F. The interplay between structure and orbitals in the chemical bonding of graphite. Chem Phys Lett 2010;496:291–5.
[32] Gambetta A, Manzoni C, Menna E, Meneghetti M, Cerullo G, Lanzani G, et al. Real-time observation of nonlinear coherent phonon dynamics in single-walled carbon nanotubes. Nature 2006;2:515–20.
[33] Lim Y-S, Yee K-J, Kim J-H, Haroz EH, Shaver J, Kono J, et al. Coherent lattice vibrations in single-walled carbon nanotubes. Nano Lett 2006;6(12):2696–700.
[34] Ma YZ, Valkunas L, Dexheimer SL, Bachilo SM, Fleming GR. Femtosecond spectroscopy of optical excitations in single-walled carbon nanotubes: evidence for exciton–exciton annihilation. Phys Rev Lett 2005;94(15):157402–5.
[35] Valkunas L, Ma Y-Z, Fleming GR. Exciton–exciton annihilation in single-walled carbon nanotubes. Phys Rev B 2006;73(11):115432–43.
[36] Ma Y-Z, Stenger J, Zimmermann J, Bachilo SM, Smalley RE, Weisman RB, et al. Ultrafast carrier dynamics in single-walled carbon nanotubes probed by femtosecond spectroscopy. J Chem Phys 2004;120(7):3368–73.
[37] Reich S, Thomsen C, Maultzsch J. Carbon nanotubes, basic concept and physical properties. Wiley; 2004. 67–82.
[38] Damnjanovic M, Milosevic I, Vukovic T, Sredanovi RM. Full symmetry, optical activity, and potentials of single-wall and multiwall nanotubes. Phys Rev B 1999;60(4):2728–39.
[39] Choi HCh, Kim SY, Jang WS, Bae SY, Park J, Kim KL, et al. X-ray photoelectron spectroscopy studies of double-walled carbon nanotube bundles synthesized using thermal chemical vapor deposition. Chem Phys Lett 2004;399:255–9.
[40] Murakami Y, Einarsson E, Edamura T, Maruyamaet S. Polarization dependence of the optical absorption of single-walled carbon nanotubes. Phys Rev Lett 2005;94(8):087402–87405.
[41] Eda BG, Lin YY, Mattevi C, Yamaguchi H, Chen HA, Chen IS, et al. Blue photoluminescence from chemically derived graphene oxide. Adv Mater 2010;22:505–9.
[42] Beard MC, Knutsen KP, Yu P, Luther JM, Song Q, Metzger WK, et al. Multiple exciton generation in colloidal silicon nanocrystals. Nano Lett 2007;7(8):2506–12.
[43] Wang S, Khafizov M, Tu X, Zheng M, Krauss TD. Multiple exciton generation in single-walled carbon nanotubes. Nano Lett 2010;10:2381–6.
[44] Murakami Y, Kono J. Existence of an upper limit on the density of excitons in carbon nanotubes by diffusion-limited exciton–exciton annihilation: experiment and theory. Phys Rev B 2009;80(3):035432–35441.
[45] Castrucci P, Tombolini F, Scarselli M, Speiser E, Del Gobbo S, Richter W, et al. Large photocurrent generation in multiwall carbon nanotubes. Appl Phys Lett 2006;89:253107–9.
[46] Shyu FL, Lin MF. Loss spectra of graphite-related systems: a multiwall carbon nanotube, a single-wall carbon nanotube bundle, and graphite layers. Phys Rev B 2000;62(12):8508–16.